AMERICAN SOCIETY FOR MICROBIOLOGY | Antimicrobial Agents and Chemotherapy®

MECHANISMS OF ACTION: PHYSIOLOGICAL EFFECTS

Check for updates

Structural Elements Involved in ATP Hydrolysis Inhibition and ATP Synthesis of Tuberculosis and Nontuberculous Mycobacterial F-ATP Synthase Decipher New Targets for Inhibitors

Chui Fann Wong,[a] Wuan-Geok Saw,[a] Sandip Basak,[a] Mio Sano,[b] Hiroshi Ueno,[b] Hwee Wen Kerk,[a] Dennis Litty,[c] Priya Ragunathan,[a] Thomas Dick,[d,e,f] Volker Müller,[c] Hiroyuki Noji,[b] Gerhard Grüber[a]

[a]School of Biological Sciences, Nanyang Technological University, Singapore, Singapore
[b]Department of Applied Chemistry, Graduate School of Engineering, The University of Tokyo, Tokyo, Japan
[c]Institute of Molecular Biosciences, Johann Wolfgang Goethe University, Frankfurt/Main, Frankfurt, Germany
[d]Center for Discovery and Innovation, Hackensack Meridian Health, Nutley, New Jersey, USA
[e]Department of Medical Sciences, Hackensack Meridian School of Medicine, Nutley, New Jersey, USA
[f]Department of Microbiology and Immunology, Georgetown University, Washington, DC, USA

Chui Fann Wong and Wuan-Geok Saw contributed equally to this article. Author order was determined in the order of structures described in this article.

ABSTRACT The F_1F_O-ATP synthase is required for the viability of tuberculosis (TB) and nontuberculous mycobacteria (NTM) and has been validated as a drug target. Here, we present the cryo-EM structures of the *Mycobacterium smegmatis* F_1-ATPase and the F_1F_O-ATP synthase with different nucleotide occupation within the catalytic sites and visualize critical elements for latent ATP hydrolysis and efficient ATP synthesis. Mutational studies reveal that the extended C-terminal domain (αCTD) of subunit α is the main element for the self-inhibition mechanism of ATP hydrolysis for TB and NTM bacteria. Rotational studies indicate that the transition between the inhibition state by the αCTD and the active state is a rapid process. We demonstrate that the unique mycobacterial γ-loop and subunit δ are critical elements required for ATP formation. The data underline that these *mycobacterium*-specific elements of α, γ, and δ are attractive targets, providing a platform for the discovery of species-specific inhibitors.

KEYWORDS ATP synthesis, bioenergetics, F-ATP synthase, nontuberculous mycobacteria, OXPHOS, tuberculosis

Mycobacteria can be separated into tuberculosis (TB)-causing mycobacteria (*Mycobacterium tuberculosis*, *M. bovis*, *M. africanum*, *M. microti*, *M. canetti*, and *M. pinnipedii* [1]) and nontuberculous mycobacteria (NTM). NTM infections are increasing in their global prevalence, morbidity, and mortality, with *M. abscessus* (*Mab*) as one of the most frequently identified rapidly growing NTM species (2, 3). *Mab* is regarded as one of the most antibiotic-resistant bacteria. Together with the emergence of multidrug-resistant (MDR) TB and the high incidence of latent TB infection (23% of world population), mycobacterial diseases present a formidable global challenge for public health (2, 4). Besides mutations in drug targets, resistance is caused by low permeability of the cell wall, biofilm formation, deficient drug-activating enzymes, target modifications, drug metabolism, or induction of drug efflux pumps (2, 5). Such pumps are either ATP- or proton-motive force (PMF) driven energy forms, generated by the electron transport chain (ETC) and the ATP forming F_1F_O-ATP synthase. The process of oxidative phosphorylation contributes mainly to the pathogens' synthesis of ATP, making the F_1F_O-ATP synthase (subunits α_3:β_3:γ:δ:ε:a:b:b':c_9)

Copyright © 2022 American Society for Microbiology. All Rights Reserved.

Address correspondence to Gerhard Grüber, ggrueber@ntu.edu.sg.

The authors declare no conflict of interest.

Received 3 August 2022
Returned for modification 2 October 2022
Accepted 28 October 2022
Published 29 November 2022

Downloaded from https://journals.asm.org/journal/aac on 21 August 2026 by 2601:189:427e:2cf0:a4d0:8707:f33a:61ff.

Downloaded from https://journals.asm.org/journal/aac on 21 August 2026 by 2601:189:427e:2cf0:a4d0:8707:f33a:61ff.

essential for the bacteria (6 to 8). Its H^+-translocating F_O domain (subunits a:c_9) uses the PMF to drive rotation of the central stalk subunits γ-ε. The latter causes sequential binding, entrapment, and phosphorylation of ADP to ATP within the nucleotide-binding and catalytic α_3:β_3-headpiece. The peripheral stalk subunits b-δ:b' smoothen transmission of power between the rotary c-ring and the α_3:β_3:γ:ε domain (9 to 12).

A special feature described for F-ATP synthases of the mycobacterial model systems, *M. smegmatis* and *M. bovis*, is their inability to establish a significant proton gradient during ATP hydrolysis due to their latent ATPase activity, preventing ATP wastage and maintaining ATP homeostasis (13 to 16). Regulative elements contributing to low ATPase activity in *M. smegmatis* can be attributed to the subunit ε (17, 18) and the *mycobacterium*-specific C-terminal domain (αCTD) of the nucleotide-binding subunit α (11, 15, 16). However, information about latent ATP hydrolysis of any NTM F_1-ATPase is missing. Importantly, both pathogens can survive in the absence of oxygen, when trapped within certain hypoxic niches in patients, where the pathogen slows its growth (19). This makes the bacteria exquisitely sensitive to any further ATP depletion and thus susceptible to drugs targeting ATP synthesis as demonstrated for the anti-TB drug bedaquiline (BDQ), being active against *Mtb*s (20), and with lower potency toward *Mab's* F-ATP synthase (21), as well as GaMF1, which kills both bacteria by targeting the *mycobacterium*-specific loop of the rotary γ-subunit (22, 23). This 12- to 14-amino-acid loop is absent in the human homologue and proposed to be an essential feature for catalysis (14, 22). However, so far, no detailed study exploring the role of this γ-loop of any recombinant mycobacterial F-ATP synthase has been described. Previously, the crystallographic structure of the *M. smegmatis* F_1-ATPase published at 4.0 Å resolution proposed an MgADP inhibitory state (24). More recently, the electron cryo-microscopy (Cryo-EM) structures of the BDQ-inhibited *M. smegmatis* F-ATP synthase have been resolved (11, 25).

Here, we describe the cryo-EM structure of the *M. smegmatis* F_1-ATPase (*Ms*F_1-ATPase) and the F_1F_O-ATP synthase (*Ms*F-ATP synthase) at defined nucleotide-occupation states. The *mycobacterium*-specific modifications of the F-ATP synthase, namely, the αCTD (15), an inserted δ-domain (10), or the extra γ-loop (14), respectively, are visualized. Rotary dynamics studies of the recombinant *M. smegmatis* ε-free complex and its mutant with the deletion of the αCTD provide first insights into the chemo-mechanical coupling and regulation mechanisms. Mutational studies of the subunits α and γ within the recombinant *M. smegmatis* F_1-ATPase and F-ATP synthase demonstrate unequivocally the importance of the αCTD and the γ-loop for latent ATP hydrolysis and ATP formation, respectively. Movements of the peripheral stalk subunit δ visualized different states of the *M. smegmatis* F-ATP synthase and underpin its function as a transfer element of elastic energy during ATP formation. Finally, the first recombinant *Mab* F_1-ATPase and its αCTD mutants highlight the overall phenomena of ATP hydrolysis inhibition and reveal differences of this domain among mycobacteria, making it a specific target for novel inhibitors to bind.

RESULTS AND DISCUSSION

Cryo-EM analysis of the *Ms*F_1-ATPase. The *Ms*F_1-ATPase used for cryo-EM studies was purified according to Wong et al. (18). No exogenous nucleotides were added prior to vitrification. We collected 2,316 movies at an accelerating voltage of 300 kV, yielding a final class of 120,114 for reconstruction (Fig. S1 in the supplemental material). The *Ms*F_1-ATPase cryo-EM structure was resolved to a nominal resolution of 3.5 Å (Fig. 1A; Fig. S1B to D; Table S2A to C). Although the density of the ε-subunit is present, the low-quality density map led to a final model of the α_3:β_3:γ complex (Fig. 1B). The presented structure reveals an F_1-ATPase where the indirect binding change mechanism proposed by Boyer was observed (26). In the three noncatalytic α-subunits, MgATP could be well modeled in the density maps (Fig. 1C). No additional density could be observed in the empty catalytic β-subunit, while MgADP occupied the remaining β-subunits (Fig. 1C). The asymmetric nucleotide occupation of the $\alpha_3\beta_3$-

Downloaded from https://journals.asm.org/journal/aac on 21 August 2026 by 2601:189:427e:2cf0:a4d0:8707:f33a:61ff.

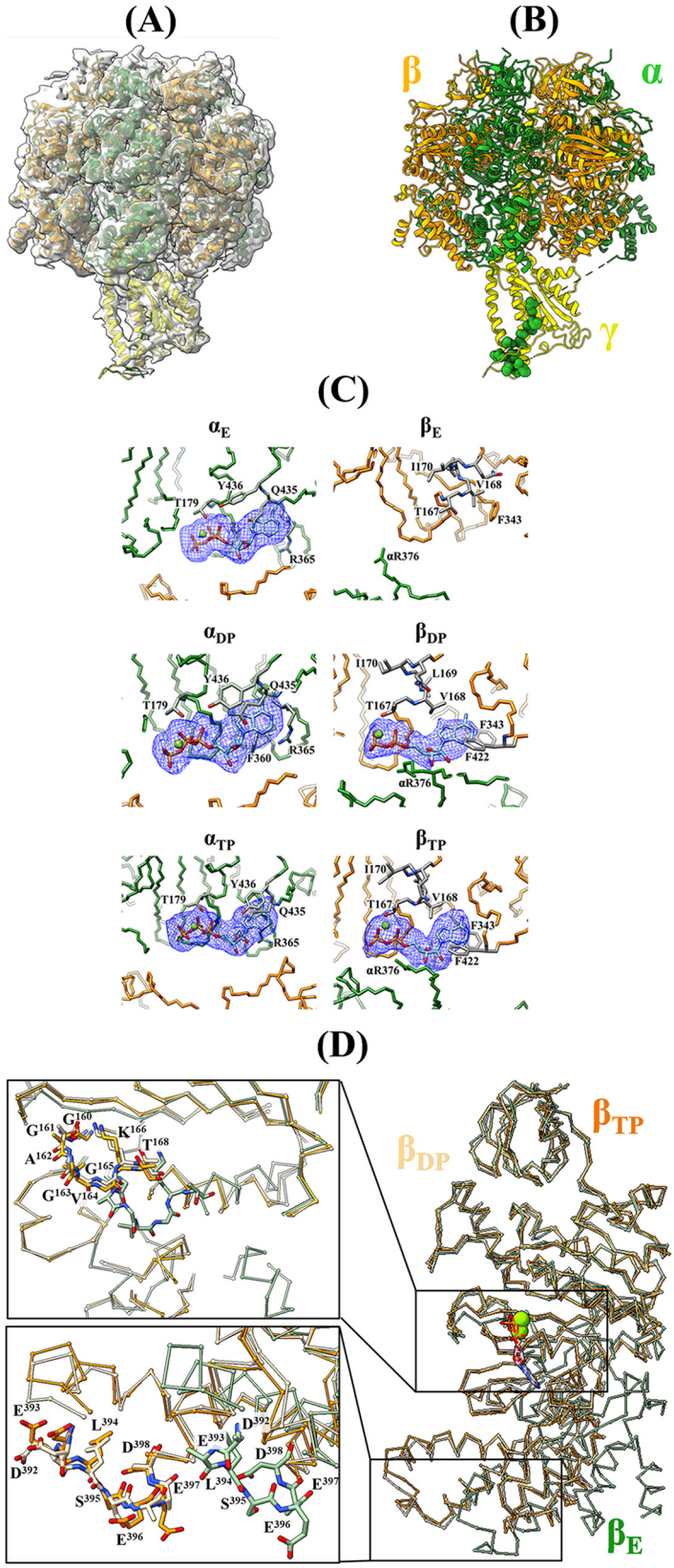

FIG 1 Structural analysis of *M. smegmatis* F_1-ATPase. (A) Superimposition of the 3.5 Å resolved cryo-EM density map and atomic model of the *Ms*F_1-α_3:β_3:γ. Weak density corresponding to the ε-subunit was removed for clarity. (B) The structural model of the F_1 α_3:β_3:γ complex, illustrated in forest green,

(Continued on next page)

Downloaded from https://journals.asm.org/journal/aac on 21 August 2026 by 2601:189:427e:2cf0:a4d0:8707:f33a:61ff.

hexamer is further illustrated in the conformational changes between the $\alpha\beta$ pairs. In the tight catalytic state ($\alpha\beta_{DP}$), the $\alpha\beta$ pairs forms a close interface, which further widens from the loose ($\alpha\beta_{TP}$) to the empty state ($\alpha\beta_{E}$) (Fig. 1D, Movie S1). Comprehensively, the $_{392}\beta$DELSEED$_{398}$ region was observed to shift by approximately 29.5 degrees from the β_{DP} to β_{E} state (Fig. 1D, bottom inset).

No significant rotation was observed between the β_{DP} and β_{TP} DELSEED region (rotation angle = 4.02 degrees), as well as the phosphate-binding loop ($_{160}$GXXXXKT$_{167}$) in the different states (Fig. 1D, top inset). The nucleotide occupation of the presented F_1-ATPase differs from the 4.0 Å crystallographic structure of the *Ms*F_1-ATPase (PDB 6FOC) (24), in which crystals have been grown in the presence of 1 mM ADP. This crystallographic structure reveals density in the β_{E} site, which could reflect either phosphate or sulphate. The nucleotide occupancy was interpreted as a possible ADP-dependent ATPase inhibitory mechanism (24).

The catalytic states of the F_1-ATPase correlates to the position of the antiparallel coiled α-helices in the γ-subunit. The latter drives the conformational changes observed in the catalytic $\alpha_3\beta_3$-hexamer (27, 28). Apart from the antiparallel α-helices that protrude into the $\alpha_3\beta_3$-hexamer (amino acids 1 to 35 and 256 to 304), the remainder of the γ-subunit forms a globular fold comprising both α-helices and β-sheets (Fig. 2A). In the current cryo-EM structure, the α-helices and β-sheets including the Rossmann fold were built (Fig. 2A). The density could be assigned to the highly polar γ_{166}DDEGDDAGADGILG$_{179}$ loop. This *mycobacterium*-specific γ-loop has been described as a novel anti-TB and anti-*Mab* compound target, leading to the inhibitor GaMF1 (22). To test whether this loop affects ATP hydrolysis of the *Ms*F_1-ATPase, the *Ms*F_1-ATPase $\Delta\gamma$166-179-mutant was engineered (Fig. 2B; Table S3). As shown in Fig. 2C, the deletion of the γ-loop did not cause any significant change in ATPase activity.

Self-inhibition mechanism of ATP hydrolysis of the mycobacterial F_1-ATPase. A second *mycobacterium*-specific structural feature includes the extended 3.5-kDa C-terminus of subunit α (αCTD, residues 514 to 549 in *Mtb* [*Mtb* αCTD] and 514 to 548 in *M. smegmatis* [*Ms* αCTD]) (15). Amino acids 514 to 549 and 540 to 549 of the *Mtb* αCTD have been predicted to form a random coil, whereby residues 526 to 539 were predicted and demonstrated by NMR spectroscopy to form an α-helix in *Mtb* (15), while former cryo-EM structures reveal a β-sheet in *M. smegmatis* (11). The recently described chromosomal deletion mutation of the α_{CTD} mutant $\Delta\alpha$514-548 stimulated ATP hydrolysis of inverted membrane vesicles (IMVs) of *M. smegmatis* (15), while fusing the *Mtb* α_{CTD} at the C-terminus of subunit α of the *Bacillus* PS3 F_1-ATPase (PS3 F_1) decreased ATPase activity of the hybrid enzyme (14). Even more, previous mutational studies of *Ms*F_1-ATPase mutants have demonstrated that deletion of the entire C-terminal 35 amino acids enhanced ATP hydrolysis 60-fold, which is similar to the activity of the PS3 F_1-ATPase (15), and that residues α514-522 and α538-549 contributed to the major suppression of ATPase activity (16). In the *Ms*F_1-ATPase cryo-EM structure presented here (Fig. 1B), additional densities in the γ-subunit can be assigned to the C-terminal residues α534 to 545 of one α subunit forming a catalytic pair with β_{Dp}. Amino acids αE534, αE536, αK539, αR541, and αK542 of this stretch interact with the γ residues γE207, γE209, and γE213 (Fig. S2).

This α–γ interaction is further stabilized by residues αE534 and αE536 with γR201 and γR202 (Fig. S2) and proposed to form the hook (αCTD) of a rachet (see details below) and thereby prevent ATP hydrolysis by blocking anticlockwise rotation of the

FIG 1 Legend (Continued)
orange, and yellow, respectively. For clarity, the extended α C-terminus residues, D534 to P545, are illustrated in green spheres. (C) In the F_1-ATPase, the nucleotide binding sites of all three α-subunits were occupied by the Mg-ATP, while in the catalytic β-subunits, no nucleotide was found in the βE subunit, and Mg-ADP was found in both βDP and βTP subunits. (D) Comparison of conformational states of the β-subunits of *Ms*F_1-ATPase performed with superimposition on the N-terminal β-barrels. In brief, the C-terminus of the different states of the β-subunits were observed to undergo slight rotation, particularly in the β_{E} state compared to the β_{DP} and β_{TP} states. The rotation angular shifts in the phosphate-binding loop ($_{160}$GXXXXKT$_{167}$) and the β $_{392}\beta$DELSEED$_{398}$ region are represented in the top and bottom insets, respectively.

Downloaded from https://journals.asm.org/journal/aac on 21 August 2026 by 2601:189:427e:2cf0:a4d0:8707:f33a:61ff.

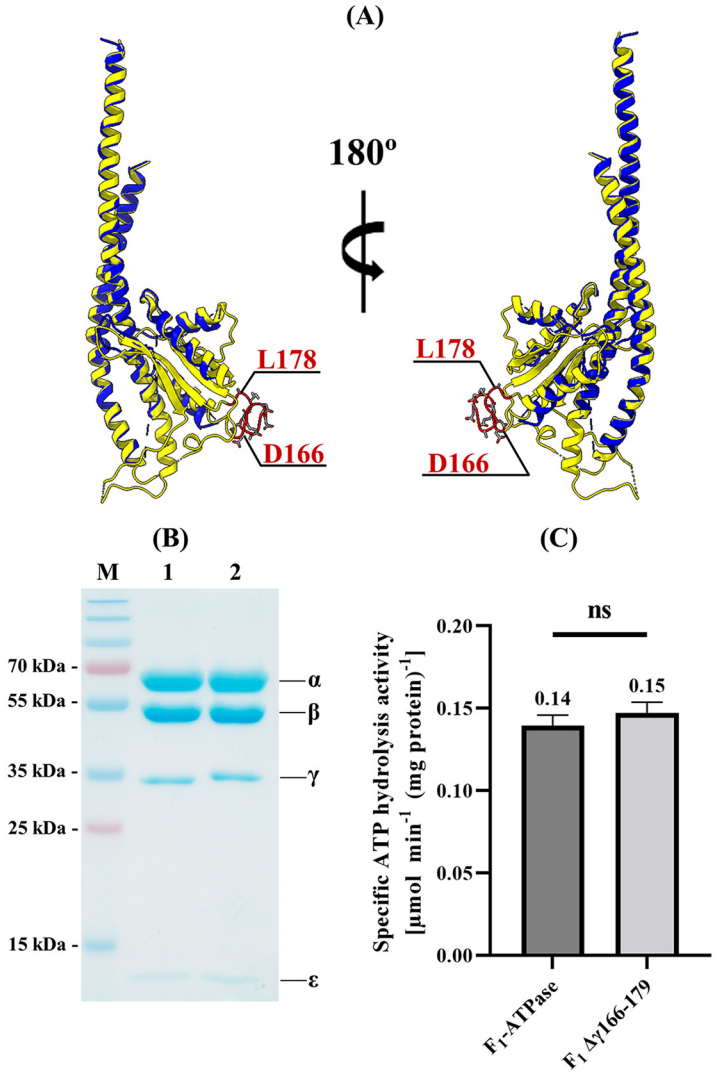

FIG 2 Analysis of the *M. smegmatis* Δγ166-179 loop. (A) Structure comparison of this cryo-EM resolved (yellow) and the crystallographic structure (PDB 6FOC) (21) (blue) γ-subunit. The globular domain and the γ166-179 loop (red) are resolved in this cryo-EM structure model. (B) SDS gel of *Ms*F_1-ATPase (lane 1) and its mutant Δγ166-179 (lane 2). M, marker. (C) ATP hydrolysis of the *Ms*F_1-ATPase and the F_1-ATPase Δγ166-179 mutant represented in bar chart. Calculated specific activities are 0.139 ± 0.002 and 0.147 ± 0.002 μmol min^{-1} (mg protein)$^{-1}$, respectively. ns indicates $P = 0.2217$. Statistical analysis of the data was performed with unpaired Student's *t* test, two-tailed with $n = 3$.

central stalk but allowing rotation in ATP synthesis direction (11, 25). In contrast, the CTDs of the remaining two α subunits are disordered, implying that α527-545 shifts from an unstructured element into a β-strand when interacting with γ210-212. Such structural alterations have also been described for the inhibitory protein IF of the mitochondrial F_1-ATPase (29), or subunit ζ in α-proteobacteria (30), whose N termini shift from an intrinsically disordered region to an inhibitory α-helix when interacting with their regulatory partners in the catalytic sites.

αCTD's interaction with γ causes intramolecular friction during rotation. To further elucidate the effect of the αCTD on rotation of the engine, we employed a single-molecule rotation assay. We used the recently generated *M. smegmatis* ε-free complex *Ms*F_1-αβγ (18), which in contrast to the wild-type (WT) *Ms*F_1-ATPase showed an increase in specific ATPase activity (Fig. 3). Cysteines were introduced in γG111 and γL231 to facilitate binding of the biotinylated beads (here labeled F_1-$\alpha\beta\gamma_{cys}$; Fig. 3A). This provided a comparable system to the well-studied TF_1 complex (αβγ). A second

Downloaded from https://journals.asm.org/journal/aac on 21 August 2026 by 2601:189:427e:2cf0:a4d0:8707:f33a:61ff.

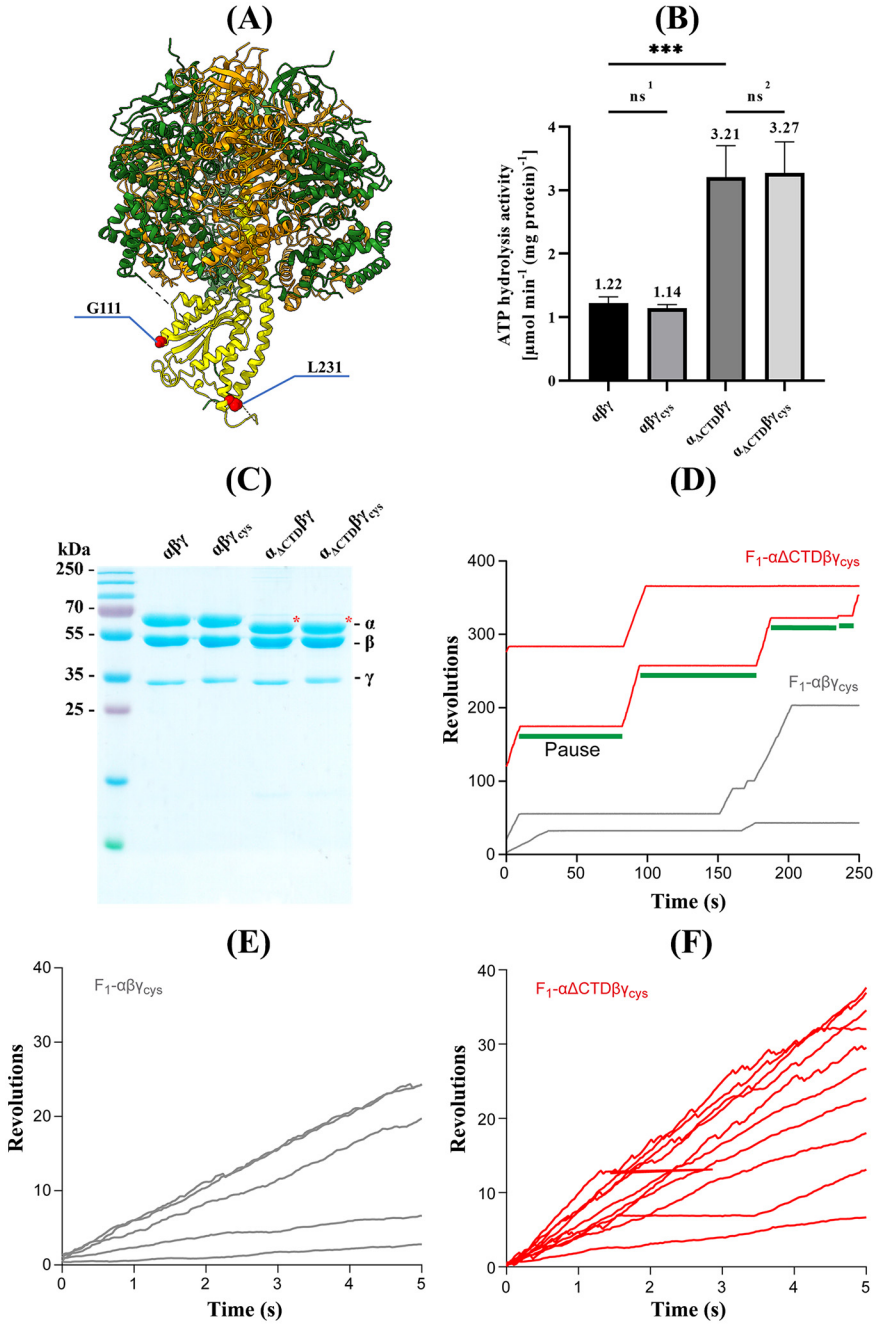

FIG 3 (A) Cysteine introductions into the *Ms*F_1-$\alpha\beta\gamma$. (B) No significant differences in ATP hydrolysis rates were observed in the mutants. The specific activities for *Ms*F_1-$\alpha\beta\gamma$, *Ms*F_1-$\alpha\beta\gamma_{cys}$, *Ms*F_1-$\alpha_{\Delta CTD}\beta\gamma$, and *Ms*$F_1$-$\alpha_{\Delta CTD}\beta\gamma_{cys}$ are 1.22 ± 0.07, 1.14 ± 0.33, 3.21 ± 0.29, and 3.27 ± 0.31 μmol min^{-1} (mg protein)$^{-1}$, respectively. Statistical analysis was performed with one-way ANOVA (analysis of variance) test, with $n = 3$. Adjusted P values are $P < 0.0004$ (***), *ns* (1) = 0.9906, and *ns* (2) = 0.9944. (C) SDS-PAGE gel of the purified mutants. The $\alpha\beta\gamma$ subunits are prominent at approximately 60, 55, and 35 kDa, respectively. In the deleted αCTD mutants, the α subunit runs lower (*). (D and E) Rotation of F_1-$\alpha\beta\gamma_{cys}$ and F_1-$\alpha_{\Delta CTD}\beta\gamma_{cys}$. (D) Pause and rotation of F_1-$\alpha\beta\gamma_{cys}$ (gray lines) and F_1-$\alpha_{\Delta CTD}\beta\gamma_{cys}$ (red lines) at 2 mM MgATP. (E and F) Time courses of rotation of F_1-$\alpha\beta\gamma_{cys}$ (gray lines, $n = 5$ molecules) and F_1-$\alpha_{\Delta CTD}\beta\gamma_{cys}$ (red lines, $n = 10$ molecules).

mutant with the deletion of the entire *Ms*αCTD (here labeled F_1-$\alpha_{\Delta CTD}\beta\gamma_{cys}$) with an ATP hydrolysis activity of 3.27 ± 0.31 μmol min^{-1} (mg protein)$^{-1}$ was generated to investigate the effect of αCTD on rotation (Fig. 3B and C).

First rotation assays with 40 nm gold colloid under nonviscous friction revealed

Downloaded from https://journals.asm.org/journal/aac on 21 August 2026 by 2601:189:427e:2cf0:a4d0:8707:f33a:61ff.

insufficient F_1-$\alpha\beta\gamma_{cys}$ rotating molecules compared to F_1-$\alpha_{\Delta CTD}\beta\gamma_{cys}$, probably due to the intrinsic autoinhibitory nature of the CTD. Therefore, magnetic beads with a diameter of about 200 to 400 nm (31) have been used in the presence of 2 mM MgATP with a recording time of 30 frames per second (fps). Smooth rotation of F_1-$\alpha\beta\gamma_{cys}$ (Movie S2; 5 molecules) and F_1-$\alpha_{\Delta CTD}\beta\gamma_{cys}$ (Movie S3; 10 molecules) rather than stepping rotation was observed (32), which may be due to the high viscous friction of the magnetic beads. Both molecules showed slow transitions between continuous rotation and intervening pauses (Fig. 3D), as previously found for TF_1 (33). The mean times for continuous rotation and pause should correspond to the lifetimes of a catalytically active and inhibition state, respectively. As shown in Table S3, the mean time for rotation and pause was 14 to 23 s and 43 to 52 s, respectively, in both molecules, revealing that a significant difference was not observed in the slow transition between rotation and pausing state of both complexes. Importantly, F_1-$\alpha\beta\gamma_{cys}$ and F_1-$\alpha_{\Delta CTD}\beta\gamma_{cys}$ differed in the rotation velocity during continuous rotation (Fig. 3E and F, Table S4, Movie S2 and S3) with a mean rotation velocity of 3.1 $\pm$ 2.2 rps and 5.2 $\pm$ 2.2 rps for F_1-$\alpha\beta\gamma_{cys}$ and F_1-$\alpha_{\Delta CTD}\beta\gamma_{cys}$, respectively. Since the rotation velocity is in principle limited by the hydrodynamic friction on rotating magnetic beads, the rotation velocity is a measure of torque that the F_1 molecule exerts. Therefore, the observed difference suggests that F_1-$\alpha\beta\gamma_{cys}$ including the αCTD generates lower torque. However, considering that the C-terminal extension is not directly involved in the torque generation process, it would be more reasonable to consider that the αCTD acts by causing intramolecular friction when interacting with the rotating γ subunit. Although the αCTD–γ interaction within the *Ms*F_1ATPase structure seems to be stable (Fig. S2), the present results suggest that the transition between inhibition state by the αCTD and the active state is a rapid process such that the rotation is seemingly slowed uniformly over all rotational angles without showing distinctive pauses.

αCTD inhibition is also conserved in NTM F_1-ATPases. Although the αCTD extension is unique to mycobacteria, it differs in amino acid composition in particular to the three *Mab* subspecies, underlined by the differences in the predicted α-helical and β-sheet content compared to other mycobacterial αCTDs (Fig. 4A and B).

To explore whether NTM F_1-ATPases also uses the same regulative αCTD, we generated the first recombinant *Mab* subsp. *abscessus* F_1-ATPase (*Mab*F_1-ATPase; α_3:β_3:γ:ε) and visualized its α_3:β_3-domain with subunit γ in top views of 2D projections of negative-stained electron micrographs (Fig. 4C). The *Mab*F_1-ATPase displayed low ATP hydrolytic activity of 0.04 μmol min^{-1} (mg protein)$^{-1}$ (Fig. 4D). Based on the secondary structure prediction (Fig. S3B), three deletion mutants, *Mab*F_1-$\alpha_{\Delta 514\text{-}548}\beta\gamma\varepsilon$, F_1-$\alpha_{\Delta 532\text{-}548}\beta\gamma\varepsilon$, and -$F_1$-$\alpha_{\Delta 542\text{-}548}\beta\gamma\varepsilon$, were generated for assessment of their roles in the inhibition of *Mab's* ATPase activity (Fig. 4D and E).

Deletion of the entire αCTD in the F_1-$\alpha_{\Delta 514\text{-}548}\beta\gamma\varepsilon$ mutant enhanced ATP hydrolysis by 32-fold (1.28 $\pm$ 0.048 μmol min^{-1} (mg protein)$^{-1}$), while the ATPase activity of the F_1-$\alpha_{\Delta 532\text{-}548}\beta\gamma\varepsilon$ and F_1-$\alpha_{\Delta 542\text{-}548}\beta\gamma\varepsilon$ mutants increased by a factor of 9 (0.36 $\pm$ 0.01 μmol min^{-1} (mg protein)$^{-1}$) and 13.5 (0.54 $\pm$ 0.05 μmol min^{-1} (mg protein)$^{-1}$), respectively, compared with the WT complex (Fig. 4D). The results illustrate that the unique αCTD is the major ATP hydrolysis inhibitory element of F-ATP synthases of both TB-causing mycobacteria and NTM. Furthermore, as shown for the *M. smegmatis* enzyme (11), the *Mab* αCTD with its specific residues and its interacting γ subunit may become an interesting inhibitor target in future, since it is not present in the human counterpart and would thus ensure lack of on-target toxicity.

Cryo-EM analysis of MgATP-saturated *M. smegmatis* F-ATP synthase. While the cryo-EM structures of the BDQ-inhibited *Ms*F-ATP synthase have been published (11, 25), we explored the structure of the *Ms*F-ATP synthase saturated with 1 mM MgATP. The *Ms*F-ATP synthase was incubated with 1 mM Mg-ATP for 5 min on ice prior to vitrification. We collected 3,663 movies, yielding a final particle set of 59,576 particles (Fig. S3A) that were subsequently sorted into three rotational states (Fig. 5A). The different rotational states correspond to the orientation of the subunit γ, alluding to different rotary catalysis positions. The final resolutions of the rotational states 1 to 3 are 4.4, 4.7,

Downloaded from https://journals.asm.org/journal/aac on 21 August 2026 by 2601:189:427e:2cf0:a4d0:8707:f33a:61ff.

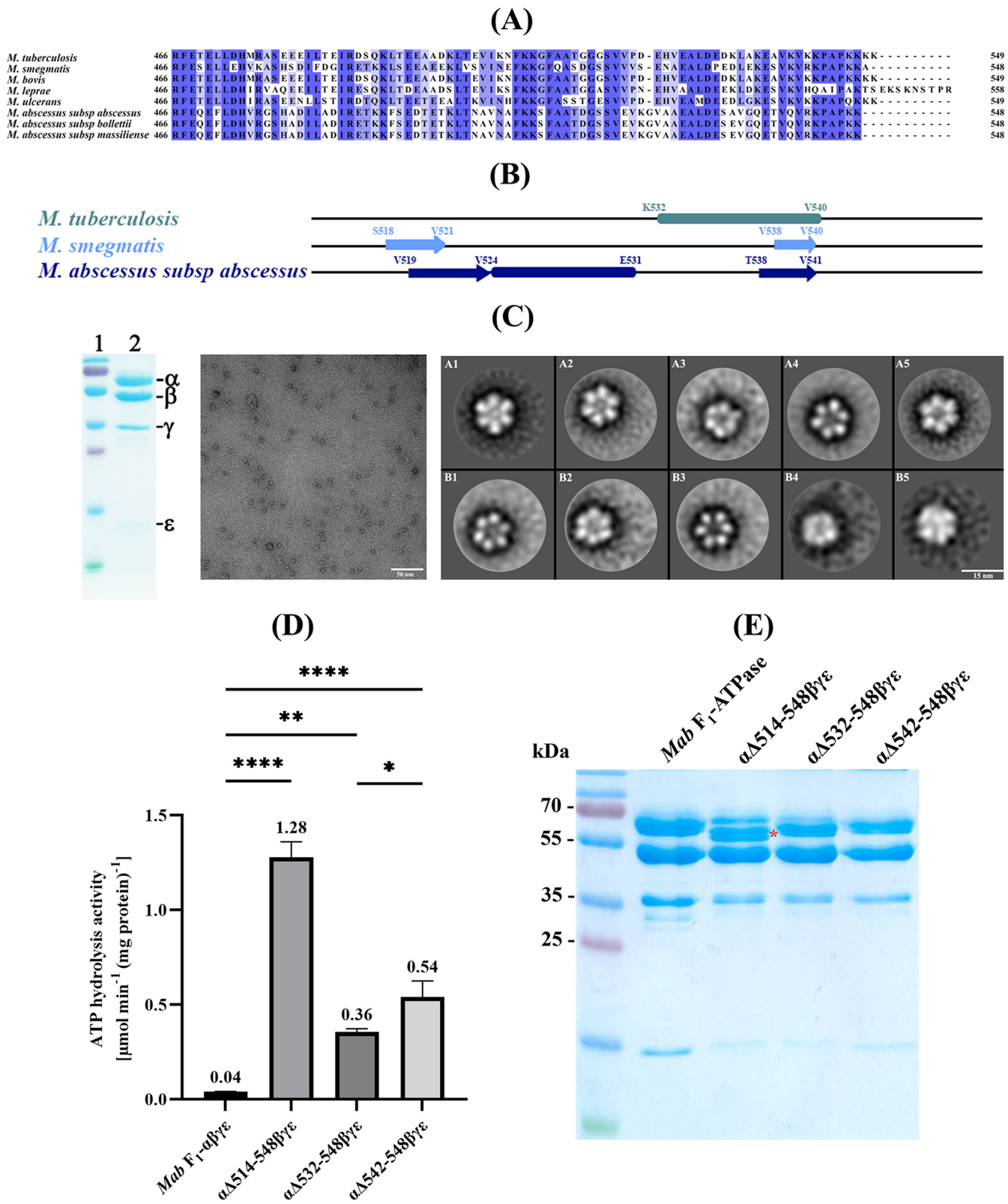

FIG 4 Characterization of the auto-inhibition element αCTD of *Mab*'s F_1-ATPase. (A) Amino acid sequence alignment of the αCTDs from different mycobacterial organisms showing significant differences in amino acid composition. The percentage of identity is presented in darker to lighter shades of blue, representing the most homologous to the least homologous. (B) Secondary structure predictions, using PREDATOR (39), of the C-terminal region of α subunit in *Mtb*, *M. smegmatis*, and *Mab*, revealing three secondary structure elements: two β-sheets formed by residues numbered 519 to 524 and 538 to 542, and one α-helix formed by residues numbered 525 to 531. Non-highlighted black lines represent random coils prediction. (C) Left, 12% SDS gel

(Continued on next page)

Downloaded from https://journals.asm.org/journal/aac on 21 August 2026 by 2601:189:427e:2cf0:a4d0:8707:f33a:61ff.

and 7.3 Å, respectively (Fig. S3A to F). The overall percentage of particles were favored toward rotational states 2 (44.2%), 1 (37.6%), and 3 (18.2%). The densities of all F-ATP synthase subunits can be visualized clearly from the maps in states 1 and 2. In state 3, the densities of the *c*-ring cannot be resolved properly in view of the low resolution. The model of *Ms*F-ATP synthase was built into the map of state 1 (Fig. 5B), using the starting model of the recently described *M. smegmatis* structure (PDB 7JG5) (11). The quality of the optimized model obtained after refinement was then evaluated using Molprobity, yielding a Molprobity score of 1.52 (Table S2C). This derived model was used as a reference for rigid body fitting into the maps of the two remaining rotational states. Like in other bacterial F-ATP synthases, the central stalk rotates by about 120° from one rotational state to another (Movie S4).

Nucleotide occupancies were observed in all nucleotide-binding sites (Fig. 5C, blue box). Like in the α subunits of the cryo-EM *Ms*F_1-ATPase (Fig. 1C) and the recently described *Ms*F-ATP synthase structures (PDB ID 7JG5 [11] and 7NJK [25]), all three α subunits bind MgATP (Fig. 5C). In the present structure, ADP was assigned in the β_E subunit and adopted a "forced open" conformation for its $\alpha\beta$-interface (Fig. 5C, red box, and Fig. S4), while in the so-called β_{TP} and β_{DP} subunits, MgATP occupied both catalytic sites and adopted a "loose" and "tight" conformation, respectively (Fig. 5C, red box). This nucleotide occupation pattern is different from the pattern determined by Guo et al. (PDB ID 7JG5) (11) with a phosphate being modeled in β_E and β_{DP}, while β_{TP} was occupied by MgATP. Such occupation may have been caused by the missing exogenous nucleotides during enzyme preparation. The occupancy of nucleotides in the β subunits within our structure also differs from the most recent structure (PDB ID 7NJK) (25), in which ADP, MgADP, and MgATP have been found in β_E, β_{TP}, and β_{TP}, respectively (Movie S5).

The αCTD and γ-loop inhibit ATP hydrolysis and synthesis, respectively. The density attributed to the extension of the α subunit was also evident in this F-ATP synthase structure. This extension was observed in α_{DP} from E531 to P545 (state 1) and from E534 to P545 (state 2), but not in the map of rotational state 3 (Fig. S5). No additional density could be observed in the α_E and α_{TP}. So far, studies using recombinant mycobacterial F_1-ATPase (reference 16 and studies above) or F_1F_O-ATP synthase (11) to explore the unique αCTD have focused on its role in self-inhibition of ATP hydrolysis. To understand if the release of this auto-inhibition affects proper function of the mycobacterial F-ATP synthase in synthesis, the recombinant *Ms*F-ATP synthase with a deletion of α514-548 (F_1F_O $\Delta\alpha$514 to 548) was generated and purified (Fig. 6A).

We used our established reconstitution protocol to detect ATP synthesis (Fig. 6B) (12). The outcome revealed a 12% decrease (29.4 $\pm$ 0.9 nmol min^{-1} (mg protein)$^{-1}$) in ATP synthesis in the reconstituted liposomes compared to the WT enzyme (33.3 $\pm$ 0.2 nmol min^{-1} (mg protein)$^{-1}$; Fig. 6B) underpinning the concept of the recently described ATP synthesis inhibitor AIMF1 by targeting the αCTD and its interaction region within the γ-subunit (34). In contrast, a major increase of ATP hydrolysis was observed in the mutant complex (Fig. 6C), showing a 16.5-fold increase compared to WT complex, consistent with previous studies (15). A so-called "fail-safe" device (25), constituted by the extra mycobacterial γ166-179 loop and also visualized in the density of the presented structure (Fig. S5B), was discussed as a second inhibitory element of ATP hydrolysis by which the peripheral stalk subunit residue *b*′R72 would form a salt bridge with either γ-loop residue D170 or D171 (25).

FIG 4 Legend (Continued)
displaying the first recombinant *Mab* F_1-ATPase (α_3:β_3:γ.ε). Middle, representative negative-stained electron micrograph of *Mab* F_1-ATPase revealing well-dispersed and individual particles. Right, 2D classes of the *Mab* F_1-ATPase showing the typical hexameric α_3:β_3 fashion with additional densities corresponding to the central stalk subunit γ. (D) ATP hydrolysis assay of the *Mab* WT F_1-ATPase and its α mutants. The adjusted *P* values for the ATPase activity differences between *Mab* F_1-$\alpha_{\Delta514\text{-}548}\beta\gamma\varepsilon$, F_1-$\alpha_{\Delta532\text{-}548}\beta\gamma\varepsilon$, and F_1-$\alpha_{\Delta542\text{-}548}\beta\gamma\varepsilon$ to the WT enzyme was determined to be $P < 0.0001$, $P = 0.0428$, and $P = 0.0045$, respectively. Comparison between the *Mab* F_1-$\alpha_{\Delta532\text{-}548}\beta\gamma\varepsilon$ and F_1-$\alpha_{\Delta542\text{-}548}\beta\gamma\varepsilon$ revealed a *P* value of ns = 0.0979. All statistical analysis was performed using one-way ANOVA test, where $n = 3$. (E) The purified proteins were assayed on a 12% SDS-PAGE gel for comparison to the WT enzyme (lane 1). The major band indicated by an * of *Mab* F_1-$\alpha_{\Delta514\text{-}548}\beta\gamma\varepsilon$ was analyzed by MALDI TOF (Table S4), confirming that this major band carries the $\alpha_{\Delta514\text{-}548}$ deletion, leading to a further migration in the SDS gel compared to the α-band of the WT F_1-ATPase.

Downloaded from https://journals.asm.org/journal/aac on 21 August 2026 by 2601:189:427e:2cf0:a4d0:8707:f33a:61ff.

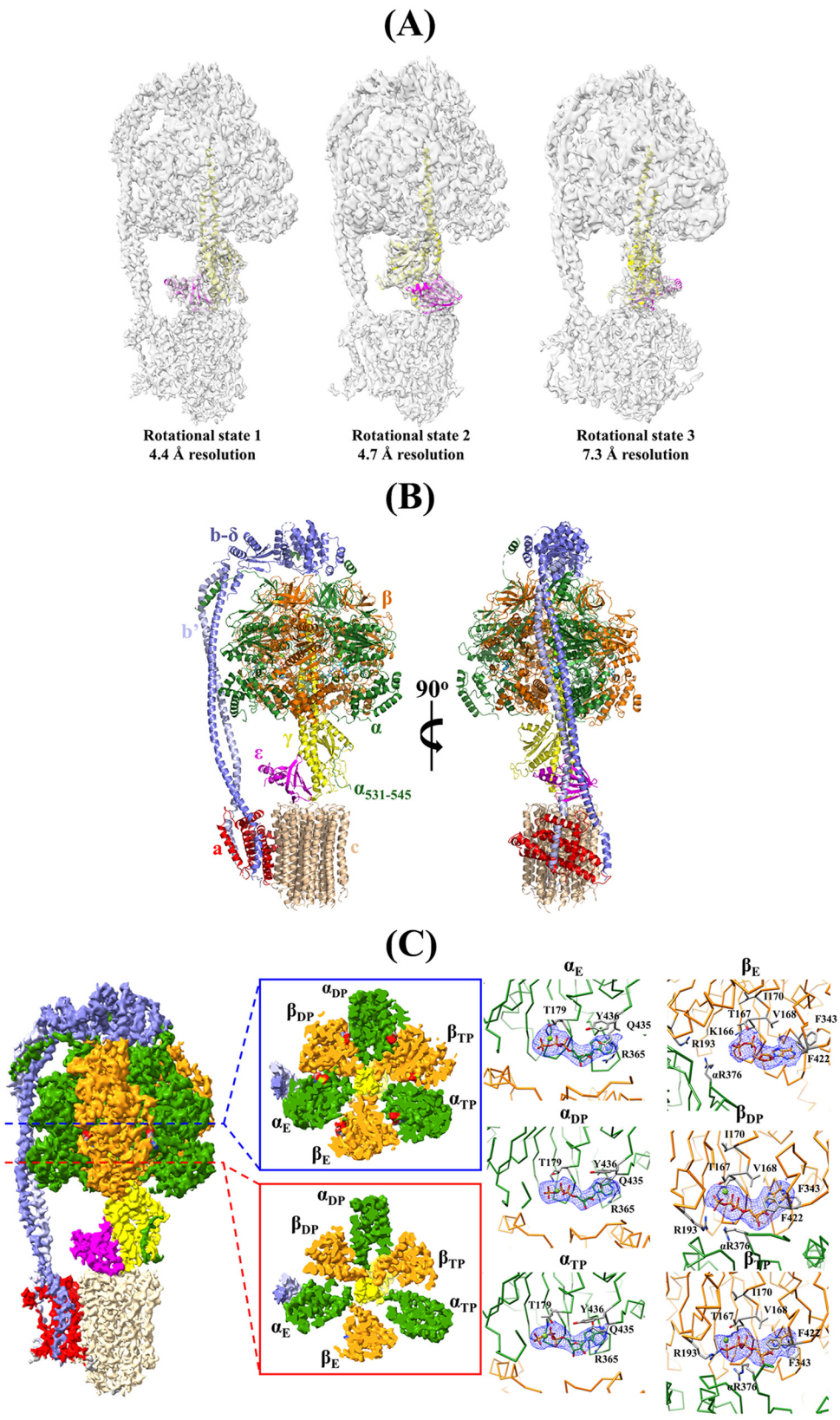

FIG 5 Structural analysis of *M. smegmatis* F-ATP synthase. (A) Cryo-EM density maps of the *Ms*F-ATP synthase in three major rotational states determined based on the rotation of the central stalk (γ, yellow cartoon; ε, magenta cartoon), with the resolutions of 4.4, 4.7, and 7.3 Å, respectively. (B) Structural model generated from cryo-EM map in the rotational state 1. (C) Cryo-EM density map of *Ms*F-ATP synthase in state 1, with the cross-

(Continued on next page)

Downloaded from https://journals.asm.org/journal/aac on 21 August 2026 by 2601:189:427e:2cf0:a4d0:8707:f33a:61ff.

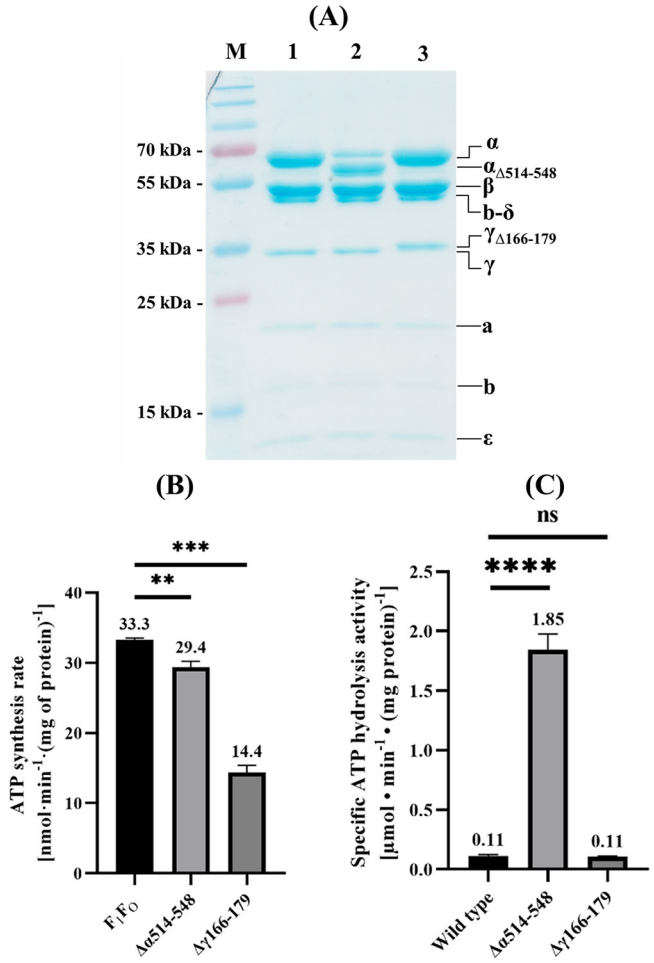

FIG 6 Characterization of the *M. smegmatis* F-ATP synthase and its mutants. (A) SDS-PAGE gel displays the subunit compositions of the purified protein complexes, including recombinant *Ms*F-ATP synthase (lane 1) and its mutants Δα514-548 (ΔαCTD) (lane 2) and Δγ166-179 (lane 3). In lane 2, the major band indicated by an * was analyzed by MALDI-TOF (Table S2 A–C) and revealed that this major band is the correct $\alpha_{\Delta 514\text{-}548}$ deletion mutant, leading to a further migration in the gel compared to the α-band of the WT F_1-ATPase. In lane 3, the subunit γ with Δγ166-179 migrated slower than WT γ, largely due to a highly charged amino acid composition from 166 to 179. M, marker. (B) ATP synthesis of the *M. smegmatis* F-ATP synthase (wild type), F_1F_O Δα514-548, and F_1F_O Δγ166-179 represented in bar chart with SD. **, $P < 0.0092$; ***, $P < 0.0001$. (C) ATP hydrolysis activity of *M. smegmatis* F-ATP synthase (wild type), F_1F_O Δα514-548, and F_1F_O Δγ166-179 represented in bar chart. Calculated specific activities are 0.112 ± 0.003, 1.846 ± 0.035, and 0.106 ± 0.002 μmol·min^{-1}·(mg protein)$^{-1}$, respectively. ****, $P < 0.0001$; ns, $P = 0.4199$. Statistical analysis of the data is performed with unpaired Student's *t* test, two-tailed, where $n = 3$.

Although the *Ms*F_1-ATPase Δγ166-179-mutant shows low ATP hydrolysis activity (Fig. 6C), we tested whether a Δγ166-179 deletion in the recombinant *Ms*F-ATP synthase with its peripheral *b′* subunit would show enhanced ATPase activity. As demonstrated in Fig. 6C, the generated *Ms*F-ATP synthase Δγ166-179 mutant revealed no difference in ATPase activity compared to the WT enzyme, highlighting that the γ-loop is not critical in ATP hydrolysis inhibition. Importantly, a decrease of 43.2% (14.4 ± 1.0 nmol min^{-1} (mg protein)$^{-1}$; Fig. 6B) in ATP synthesis was observed for the recombinant F-ATP synthase Δγ166-179 mutant, which is in line with the 54% ATP synthesis reduction measured for the chromosomal Δγ166-179 deletion mutation of *M. smegmatis* IMVs determined preciously (14).

FIG 5 Legend (Continued)
sections of (blue box) nucleotide binding site (red surface) and (red box) C-terminal domain of $\alpha\beta$-hexamer. In the F-ATP synthase, the nucleotide binding sites of all three noncatalytic α subunits were occupied by the Mg-ATP, while in the catalytic β subunits, ADP was assigned in the β_E subunit and Mg-ATP in both β_{DP} and β_{TP}.

Downloaded from https://journals.asm.org/journal/aac on 21 August 2026 by 2601:189:427e:2cf0:a4d0:8707:f33a:61ff.

Taken together, the results suggest that while the *mycobacterium*-specific αCTD prevents the central stalk mainly to rotate in the ATP hydrolysis direction, the mycobacterial γ-loop insertion affects rotation in the ATP synthesis direction, possibly via the proposed positively charged *b*′R72 and the negatively charged γD170/γD171, a pattern conserved across all mycobacterial species.

Recently, the anti-TB F-ATP synthase inhibitor GaMF1, which interacts with several residues of the γ-loop (22), has been repurposed as an anti-*Mab* F-ATP synthase inhibitor that is bactericidal and revealed enhanced anti-*Mab* activity in combination with the anti-*Mab* drugs clofazimine, rifabutin, or amikacin (23), demonstrating that the mycobacterial γ-loop is an attractive mycobacterial-wide drug target.

Movements of subunit δ, a mycobacterial-wide inhibitor target. As demonstrated for the subunits α and γ, differences in amino acid composition of the mycobacterial enzyme, compared to other prokaryotic or human counterparts, paved avenues for the discovery of molecules interfering with various regulative mechanisms of this F-ATP synthase (see above and references 22, 23, and 34). In this context, the mycobacterial peripheral stalk subunit δ displays a unique N-terminal 111-residue extension (10, 35).

Mutational studies of subunit δ in the recombinant *M. smegmatis* F-ATP synthase have highlighted the importance of this subunit for effective catalysis (12) and has indicated the critical communication for smooth transfer of elastic energy between the fused N-terminal residues of δ and the C-terminus of the peripheral stalk subunit *b*, as well as the N-terminus of subunit α during rotation. Superimposition of the three models with alignments performed on subunit *a* showed slight movements of the peripheral stalk (Fig. S8A, side view) and significant movements of subunit δ (Fig. 7A and B, top view) with its noncanonical N-terminal domain (NTD) (helices α3 to α8), the central domain (CD; helices α9 to α14), and the CTD (β1 to β4 and α15 to α16). Such movement also includes α-helices 3 and 4 with residues δR171, δR171G, δR177Q, and δQ178R demonstrated to be important for ATP synthesis (12). This area has recently been identified as a novel compound target, leading to the F-ATP synthase hit molecule DeMF1, which inhibits NADH-driven ATP synthesis of *M. smegmatis* IMVs with a half-maximal inhibitory concentration (IC_{50}) of 0.5 μM (12). Its inhibitory potency has also been demonstrated in the reconstituted recombinant *Ms*F-ATP synthase (12). Targeting of the δ subunit demonstrates the potential to advance subunit δ's flexible coupling as a new area for the development also of NTM F-ATP synthase inhibitors, which is confirmed by the 43% ATP synthesis inhibition of *Mab* IMVs in the presence of 500 μM DeMF1 (Fig. 7C).

Although with 1,000-fold lower potency, this result underlines the druggability of mycobacterial subunit δ. The sequence alignment of the mycobacterial δ subunit (Fig. 7D) reveals that the DeMF1's interacting residues δR177, -L180, -E366, -R371, -R372, -E374, and -R403 are similar in *Ms* and *Mab*. Amino acid polymorphisms were observed for δR171, -R173, -Q178, -H273, and -G373, explaining the 1,000-fold lower efficiency in *Mab* IMVs. These data pave the way for future medical chemistry efforts for new leads targeting mycobacterial subunit δ with specificities to the class of TB-causing mycobacteria and NTM.

Conclusion. The cryo-EM structures of the *Ms*F_1-ATPase and the -F_1F_O-ATP synthase revealed different nucleotide occupation within the catalytic sites, going along with movements of the C-terminal domain of the catalytic β subunits and the central stalk element. To maintain PMF and ATP homeostasis, TB-causing mycobacteria and NTM "invented" the αCTD. Deletion of this domain resulted in stimulated ATPase activity of the motor and minor inhibition in ATP synthesis, highlighting its role in preventing wastage of ATP and maintaining PMF. The αCTD binds to the rotating γ-subunit, leading to intramolecular friction (Fig. 8) and, together with subunit ε, inhibits ATP hydrolysis. Rotational studies indicated that the transition between the inhibition state by the αCTD and the active state is a rapid process in which rotation slows uniformly over all rotational angles. In comparison, the unique mycobacterial γ-loop does not affect ATP hydrolysis inhibition either in the F_1-ATPase or in the entire F-ATP synthase but is a fundamental element for ATP formation (Fig. 8). Movements of the peripheral stalk, in particular subunit δ including the

Downloaded from https://journals.asm.org/journal/aac on 21 August 2026 by 2601:189:427e:2cf0:a4d0:8707:f33a:61ff.

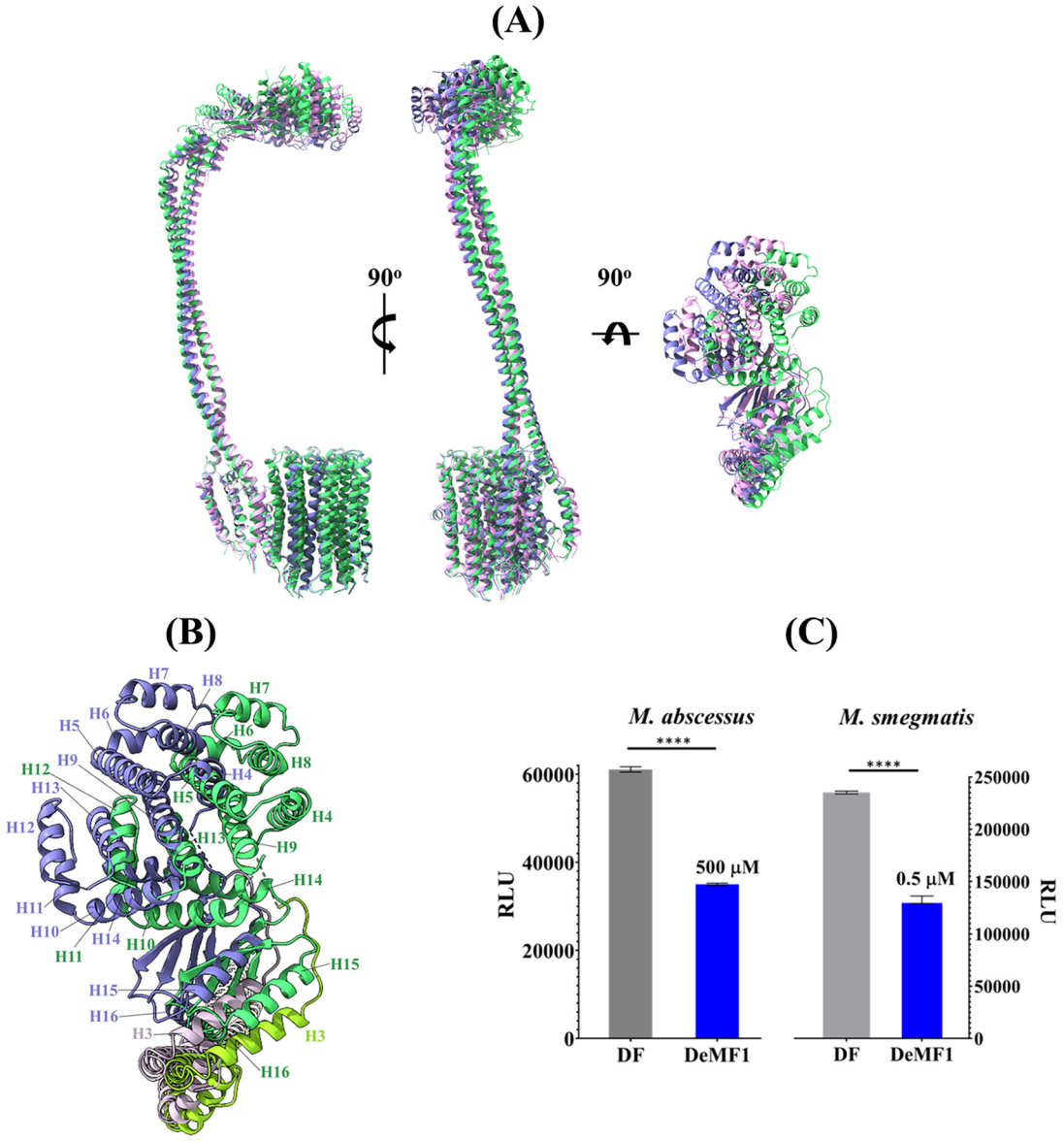

(D)

```
                                                
```

Downloaded from https://journals.asm.org/journal/aac on 21 August 2026 by 2601:189:427e:2cf0:a4d0:8707:f33a:61ff.

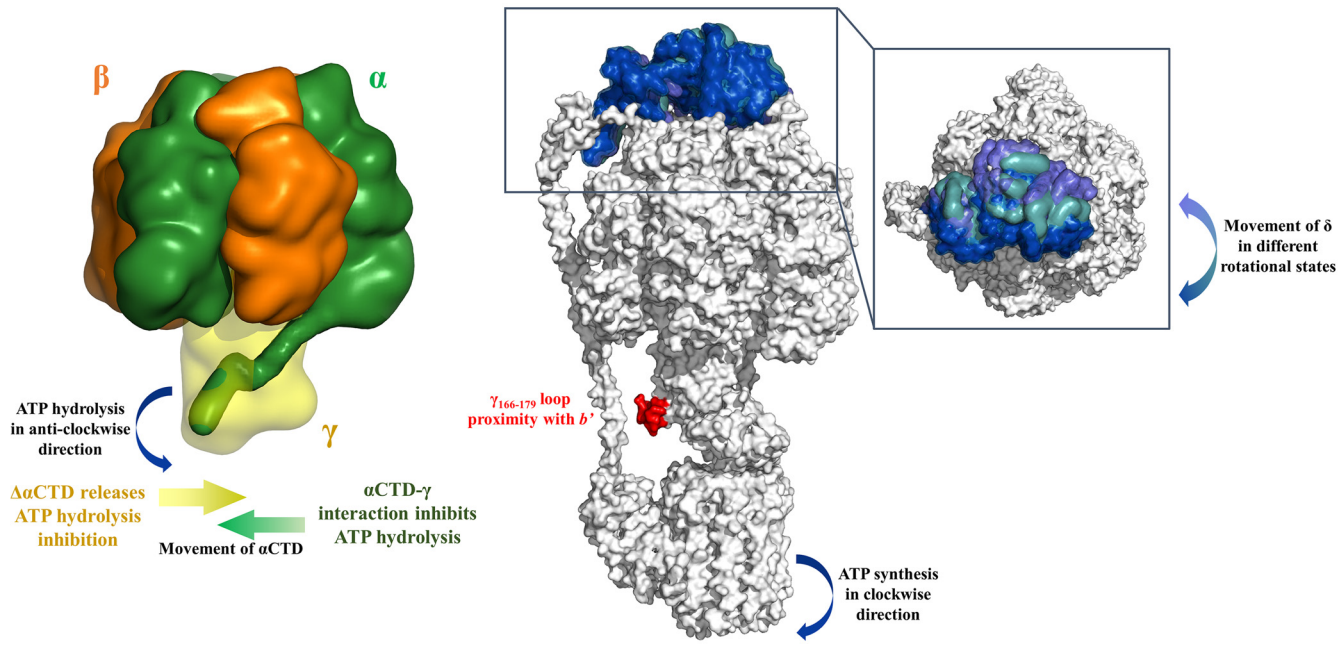

FIG 8 Summary cartoon of the data presented. The cryo-EM structures of the *Ms*F_1-ATPase and the *Ms*F_1F_O-ATP synthase have been resolved and showed different nucleotide occupation within the catalytic sites. TB-causing mycobacteria and NTM "invented" the αC-terminal extension (left) binding to the central and rotating subunit γ leading to intramolecular friction and inhibition of ATP hydrolysis. The cryo-EM structure of the *Ms*F_1F_O-ATP synthase reveals the unique mycobacterial γ-loop, which is a fundamental element for ATP synthesis. Movements of the peripheral stalk subunit δ including the *mycobacterium*-specific noncanonical NTD have been resolved. Such movements provide the smooth transmission of power caused be the rotary *c*-ring and central stalk. The mycobacterial δNTD is being discussed as an ideal anti-TB and anti-NTM inhibitor target.

mycobacterium-specific noncanonical NTD, provide the smooth transmission of power caused be the rotary *c*-ring and central stalk, which is essential for ATP synthesis (Fig. 8). The αCTD (16), the γ-loop (14), and the δNTD (12) have been described as novel anti-TB targets with new anti-TB inhibitors to bind (Fig. 8) (12, 22, 34). Although different in amino-acid composition and predicted secondary structure like in the case of αCTD (Fig. 4A and B), the data presented underline that these three *mycobacterium*-specific elements are important for F-ATP synthase's regulation and mechanisms, and ideal anti-NTM inhibitor targets, providing the platform for species specific medical chemistry efforts.

MATERIALS AND METHODS

Generation of *M. smegmatis* F_1 $\alpha\beta\gamma$ mutants for single-molecule rotational assay. To allow binding of the biotinylated beads, G111 and L231 in the γ-subunit were mutated to cysteines, generating the *Ms*F_1-$\alpha\beta\gamma_{G111C/L231C}$ mutant (labeled as the *Ms*F_1-$\alpha\beta\gamma_{cys}$ here). To observe rotational differences between the latent *Ms*F_1-$\alpha\beta\gamma_{cys}$ and the enzymatically active $\alpha\Delta$514-548 complex, a deletion from amino acids 514 to 548 was introduced to the *Ms*F_1-$\alpha\beta\gamma_{cys}$ mutant, generating the *Ms*F_1-$\alpha_{\Delta514\text{-}548}\beta\gamma_{G111C/L231C}$ (labeled as the *Ms*F_1-$\alpha_{\Delta CTD}\beta\gamma_{cys}$ here). Both mutants were generated via site-directed mutagenesis, with their relevant primers and templates listed in Table S2. The respective plasmids were amplified using KAPA HiFi DNA polymerase (Kapa Biosystems; Wilmington, MA, USA). PCR products were subsequently treated with DpnI prior to transformation in *E. coli* TOP10 cells. Plasmids were extracted using GeneJET Plasmid Miniprep kit (ThermoFisher Scientific; Waltham, MA, USA), and DNA sequencing (Bio Basic Asia Pacific, Singapore) was performed to confirm the integrity of the plasmid. Plasmids carrying the gene of

FIG 7 Legend (Continued)
(H3) can be seen from the top view, while subunit δ is composed of 13 α-helices (H4 to H16) and four β-sheets lying between H14 and H15. (C) Inhibition of ATP synthesis by DeMF1 using *M. abscessus* and *M. smegmatis* IMVs with NADH as substrate represented in bar chart with SD. The gray bar shows drug free. ****, $P < 0.0001$. Statistical analysis of the data was performed with *t* test with $n = 3$. (D) Amino acid sequence alignment of the fused b–δ subunits from different mycobacterial species revealing significant differences in amino acid composition. The calculation of the percentage of identity was performed and showed in darker to lighter shades of blue, representing the most homologous to the least homologous. While DeMF1 interacting residues δR177, -L180, -E366, -R371, -R372, -E374, and -R403 are similar in *Ms* and *Mab* (*), amino acid polymorphisms were observed for δR171, -R173, -Q178, -H273, and -G373 (*).

Downloaded from https://journals.asm.org/journal/aac on 21 August 2026 by 2601:189:427e:2cf0:a4d0:8707:f33a:61ff.

interest were then transformed into *M. smegmatis* mc^{2}4517 electrocompetent cells for large-scale protein production and purification (18). Protein purification was performed as previously described (18). For downstream biotinylation assays, 5% glycerol was added to the purified sample and subsequently concentrated to 5 μM with a 100-kDA Centricon (Millipore; Burlington, WA, USA) prior to usage.

Single-molecule rotation assay. The introduced cysteines on the γ-subunit of *Ms*F$_1$-$\alpha\beta\gamma_{cys}$ and *Ms*F$_1$-$\alpha_{\Delta CTD}\beta\gamma_{cys}$ were biotinylated to attach magnetic beads as an optical probe. The rotation assay was performed as described previously using magnetic beads with slight modifications (31). Briefly, basal buffer (50 mM MOPS, pH 7.0, 50 mM KCl, 2 mM $MgCl_2$, 5 mg/mL BSA) was infused into the flow cell. After 10 min incubation, ~100 nM *Ms*F$_1$-$\alpha\beta\gamma_{cys}$ or *Ms*F$_1$-$\alpha_{\Delta CTD}\beta\gamma_{cys}$ dissolved in basal buffer was infused into the flow cell. After 10 min incubation, unbound enzyme was washed out with basal buffer, and magnetic beads were infused in the rotation assay buffer. After 10 min of incubation, unbound beads were washed out with rotation buffer (50 mM MOPS, pH 7.0, 50 mM KCl, 2 mM $MgCl_2$, indicated concentrations of ATP) containing an ATP-regenerating system (2 mM phosphoenolpyruvate, 100 μg/mL pyruvate kinase). The rotations were visualized on a phase-contrast microscope (IX-70; Olympus) with a 100× objective lens at 30 fps (FC300M; Takex). The rotation assay was performed at 23 ± 2°C.

Generation of *Mab* WT F$_1$-ATPase and its mutants. The *atp* operon encoding *Mab* F$_1$-ATPase was amplified from the genomic DNA of *Mycobacterium abscessus* subsp. *abscessus* (strain ATCC 19977; GenBank: CU458896.1) using the primers listed in Table S3. The operon was incorporated as previously described (18). In brief, overlapping regions of the vector pYUB1049 and the *Mab* F$_1$-ATPase (atp*AGDC*) were designed for PCR amplification. Amplified fragments of both the genomic DNA and the vector were then assembled with NEBuilder HiFi DNA Assembly. Thereafter, the plasmid (pYUB1049-*Mab*F$_1$) was transformed into *E. coli* TOP10 cells for plasmid amplification. Plasmid extraction and DNA sequencing were performed to confirm the integrity of the plasmid. After obtaining the plasmid with the right gene of interest, a His$_6$ tag was introduced in the N-terminus of the β-subunit via site-directed mutagenesis. The primers utilized for His$_6$ tag insertion were 5′-AAT Gca tca cca tca cca tca tAC CGC ACC AAC TGC TAA CAA GAC-3′ and 5′-GTa tga tgg tga tgg tga tgC ATT ACT CGT CTC TTC TCG TTC TCT AGT G-3′. After PCR amplification, the amplified product was treated with DpnI to remove leftover template. Finally, treated DNA samples were transformed into *E. coli* TOP10 cells for plasmid amplification, as mentioned before. Plasmids carrying the inserted His$_6$ tag were then verified through DNA sequencing.

Mutational studies involving the α C-terminus deletion were performed utilizing the template pYUB1049-*Mab*F$_1\alpha\beta\gamma\varepsilon$. Site-directed mutagenesis was performed to generate the *Mab* F$_1$-$\alpha\Delta\alpha$514-548$\beta\gamma\varepsilon$, -$\alpha\Delta$532-548$\beta\gamma\varepsilon$, and -$\alpha\Delta$542-548$\beta\gamma\varepsilon$ mutants using primers listed in Table S3. Amplified PCR products were treated like in the case of the insertion of the His$_6$ tag. Verification of plasmids carrying the desired mutations was then performed with DNA sequencing.

Purification of *Mab* WT F$_1$-ATPase and its mutants. Plasmids verified to carry the desired gene of interest were transformed into electrocompetent *M. smegmatis* mc^{2}4517. Transformed cells were plated on 7H10 agar plates supplemented with 50 μg/mL of both kanamycin and hygromycin. Single colonies were picked and inoculated into an autoinduction medium (ZYP-5052) (18) supplemented with 50 μg/mL of both kanamycin and hygromycin. Cells were incubated at 37°C, 180 rpm for 72 h, prior to harvesting. For harvesting, cells were spun down via centrifugation at 4°C, 3,648 × *g* for 20 min.

Harvested cells were resuspended in buffer A (50 mM Tris/HCl, pH 7.5, 150 mM NaCl, 15% glycerol, 2 mM Pefabloc). Resuspended cells were lysed via sonication 3 times at 25% with 1 min intervals. After sonication, cells were further ruptured with LM20 Microfluidizer (Microfluidics, Westwood, MA, USA) at 13,000 lb/in^2, 3 times. Cell lysate was then clarified using ultracentrifugation at 150,000 × *g*, for 45 min. Next, the supernatant was incubated with Ni-NTA Agarose (Qiagen Science, Germantown, MD, USA) for 1 h at 4°C. His$_6$-tagged proteins were eluted with increased step-gradient imidazole concentrations from 0 mM to 250 mM in buffer A. Eluted fractions containing the desired protein was pooled and applied on an ion-exchange column (ResQ, 1 mL; GE Healthcare, Chicago, IL, USA) with the following buffers: 50 mM Tris, pH 7.5, 10% glycerol (vol/vol) and 50 mM Tris, pH 7.5, 1 M NaCl, and 10% glycerol. Linear gradient salt elution was performed from 150 to 500 mM NaCl at a flow rate of 1 mL/min. For the α C-terminal deletion mutants, a step-gradient salt elution was utilized to resolve the elution peaks. Samples were concentrated, wherever necessary, with a 100 kDa-cutoff Centricon (Millipore, Burlington, WA, USA) at 4000 × *g* centrifugal speed.

Generation of the *M. smegmatis* F-ATP synthase mutants for reconstitution in liposomes. *M. smegmatis* F-ATP synthase $\Delta\alpha$514-548 (identified as *Ms* F-ATP synthase $\Delta\alpha$CTD here) and *Ms* F-ATP synthase $\Delta\gamma$166-179 were generated via site-directed mutagenesis with primers and its template listed in Table S3. Detailed description of the generation of the template pYUB1049-*Ms*F-ATP synthase can be found in Saw et al. (36). The respective plasmids were amplified using KAPA HiFi DNA polymerase. PCR products were subsequently treated with DpnI prior to transformation in *E. coli* TOP10 cells. Plasmids were extracted using GeneJET Plasmid Miniprep kit (ThermoFisher Scientific, Waltham, MA, USA), and DNA sequencing (Bio Basic Asia Pacific, Singapore) was performed to confirm the integrity of the plasmid. Plasmids carrying the gene of interest were then transformed into *M. smegmatis* mc^{2}4517 electrocompetent cells for large-scale protein production and purification (37). Protein purification was performed as previously described (36).

Continuous ATP hydrolysis assay. Continuous ATP hydrolysis assay performed on all mutants described above was performed as previously described (38). For all ATP hydrolysis measurements, no sample dilution was performed, and data were collected in triplicates. Detailed description of the analysis of specific activities of the enzymes may be found in Wong et al. (18).

Reconstitution and ATP synthesis assay of the recombinant *M. smegmatis* F-ATP synthase and its mutants. Reconstitution experiments and ATP synthesis assays for the *Ms* F-ATP synthase and its mutants $\Delta\alpha$CTD and $\Delta\gamma$166-179 were performed as previously described by Harikishore et al. (12).

Preparation of *Mab* IMVs and ATP synthesis. To purify inverted membrane vesicles (IMVs) of *Mab* for ATP synthesis, cells were grown overnight at 37°C in 7H9 medium supplemented with 10% Bovine albumin, dextrose and catalase (ADC), 0.2% glycerol, and 0.05% Tween 80 until they reached an attenuance at 600 nm of 0.6 to 0.7. The culture was expanded in 200 mL supplemented 7H9 medium and grown in 1-L shake flasks (180 rpm) until it reached an attenuance at 600 nm of 0.6 to 0.7. This culture was used to inoculate a 500-mL culture that was then grown overnight in 2-L shake flasks (180 rpm) until it reached an attenuance at 600 nm of 0.6 to 0.7. Approximately 5 g (wet weight) of WT *Mab* was resuspended in 20 mL membrane preparation buffer (50 mM MOPS, 2 mM $MgCl_2$, pH 7.5) containing EDTA-free protease inhibitor cocktail (one tablet per 20 mL buffer, Roche) and 1.2 mg · mL^{-1} lysozyme. The suspension was stirred at room temperature for 45 min and additionally supplemented with 300 μL of 1 M $MgCl_2$ and 50 μL DNase I. Stirring was continued for another 15 min at room temperature. All subsequent steps were performed on ice. Cells were lysed by three passages through an ice-cooled microfluidizer (Microfluidics, Westwood, MA, USA) at 18,000 lb/in^2. The suspension containing lysed cells was centrifuged at 4,200 $\times$ *g* at 4°C for 20 min. The supernatant containing the membrane fraction was further subjected to ultracentrifugation at 45,000 $\times$ *g* at 4°C for 1 h. The supernatant was discarded, and the precipitated membrane fraction was resuspended in membrane preparation buffer containing 15% glycerol, separated into aliquots, snap-frozen, and stored at −80°C. The concentrations of the proteins in the vesicles were determined by the bicinchoninic acid assay (BCA; Pierce, Waltham, MA, USA).

ATP synthesis was measured in flat-bottomed white 96-well microtiter plates (Corning, Corning, NY, USA). The reaction mix (50 μL) comprised assay buffer (50 mM MOPS, pH 7.5, 10 mM $MgCl_2$) containing 10 μM ADP, 250 μM P_i, and 1 mM NADH. The concentration of P_i was adjusted by addition of 100 mM KH_2PO_4 to the assay buffer. ATP synthesis was started by adding *Mab* IMVs at a final concentration of 5 μg · mL^{-1}. The reaction mixture was incubated at room temperature for 30 min before adding 50 μL CellTiter-Glo reagent, followed by incubation for another 10 min in the dark at room temperature. The luminescence produced, which correlates with the amount of ATP synthesized, was measured by an Infinite 200 Pro plate reader (Tecan; DKSH, Zurich, Switzerland), using the following parameters: luminescence; integration time, 500 ms; attenuation, none.

Data availability. All relevant data are available from the authors.

Structural data that support the findings of this study are openly available in PDB at https://www.rcsb.org and EM Data Bank at https://www.ebi.ac.uk/emdb/. *M. smegmatis* F_1-ATPase: PDB ID 7Y5A, EMDB ID EMD-33614. *M. smegmatis* F-ATP synthase structures: PDB ID 7Y5B, EMDB ID EMD-33615 (rotational state 1); PDB ID 7Y5C, EMDB ID EMD-33616 (rotational state 2); and PDB ID 7Y5D, EMDB ID EMD-33617 (rotational state 3).

SUPPLEMENTAL MATERIAL

Supplemental material is available online only.

SUPPLEMENTAL FILE 1, PDF file, 1.5 MB.

SUPPLEMENTAL FILE 2, MOV file, 10.8 MB.

SUPPLEMENTAL FILE 3, MOV file, 4.2 MB.

SUPPLEMENTAL FILE 4, MOV file, 4.9 MB.

SUPPLEMENTAL FILE 5, MOV file, 10.2 MB.

SUPPLEMENTAL FILE 6, MOV file, 9.9 MB.

ACKNOWLEDGMENTS

This work as well as the PhD scholarship of C.F.W. was supported by the National Research Foundation (NRF) Singapore, NRF Competitive Research Program (CRP), grant award number NRF-CRP18-2017-01. The authors acknowledge the use of the EM facility at the NTU Institute of Structural Biology.

C.F.W., W.-G.S., H.U., H.N., and G.G. designed the experiments; C.F.W., W.-G.S., S.B., H.U., H.W.K., D.L., P.R., and G.G., formal analysis; C.F.W., W.-G.S., S.B., M.S., H.W.K., D.L., and P.R., investigation; C.F.W., W.-G.S., H.U., H.N., and G.G., writing—original draft; all authors, writing—review and editing; T.D., V.M., H.N., and G.G., funding acquisition.

We declare no competing interests.

REFERENCES

1. Addo K, Owusu-Darko K, Yeboah-Manu D, Caulley P, Minamikawa M, Bonsu F, Leinhardt C, Akpedonu P, Ofori-Adjei D. 2007. Mycobacterial species causing pulmonary tuberculosis at the Korle Bu teaching hospital, Accra, Ghana. Ghana Med J 41:52–57. https://doi.org/10.4314/gmj.v41i2.55293.
2. Luthra S, Rominski A, Sander P. 2018. The role of antibiotic-target-modifying and antibiotic-modifying enzymes in *Mycobacterium abscessus* drug resistance. Front Microbiol 9:2179. https://doi.org/10.3389/fmicb.2018.02179.
3. Johansen MD, Herrmann JL, Kremer L. 2020. Non-tuberculous mycobacteria and the rise of *Mycobacterium abscessus*. Nat Rev Microbiol 18:392–407. https://doi.org/10.1038/s41579-020-0331-1.
4. WHO. 2021. Global tuberculosis report 2021. World Health Organization, Geneva, Switzerland.
5. Remm S, Earp JC, Dick T, Dartois V, Seeger MA. 2022. Critical discussion on drug efflux in *Mycobacterium tuberculosis*. FEMS Microbiology Rev 46:fuab050. https://doi.org/10.1093/femsre/fuab050.

Downloaded from https://journals.asm.org/journal/aac on 21 August 2026 by 2601:189:427e:2cf0:a4d0:8707:f33a:61ff.

Downloaded from https://journals.asm.org/journal/aac on 21 August 2026 by 2601:189:427e:2cf0:a4d0:8707:f33a:61ff.

6. Sassetti CM, Boyd DH, Rubin EJ. 2003. Genes required for mycobacterial growth defined by high density mutagenesis. Mol Microbiol 48:77–84. https://doi.org/10.1046/j.1365-2958.2003.03425.x.
7. Cook GM, Greening C, Hards K, Berney M. 2014. Energetics of pathogenic bacteria and opportunities for drug development. *In* Poole RK (ed), Advances in microbial physiology, 1st ed. Academic Press, New York, NY.
8. Saw W-G, Wu M-L, Ragunathan P, Biuković G, Lau A-M, Shin J, Harikishore A, Cheung C-Y, Hards K, Sarathy JP, Bates RW, Cook GM, Dick T, Grüber G. 2019. Disrupting coupling within mycobacterial F-ATP synthases subunit ε causes dysregulated energy production and cell wall biosynthesis. Sci Rep 9:16759. https://doi.org/10.1038/s41598-019-53107-3.
9. Preiss L, Langer JD, Yildiz Ö, Eckhardt-Strelau L, Guillemont JEG, Koul A, Meier T. 2015. Structure of the mycobacterial ATP synthase F_o rotor ring in complex with the anti-TB drug bedaquiline. Sci Adv 1:e1500106. https://doi.org/10.1126/sciadv.1500106.
10. Kamariah N, Huber RG, Nartey W, Bhushan S, Bond PJ, Grüber G. 2019. Structure and subunit arrangement of mycobacterial F_1F_O ATP synthase and novel features of the unique mycobacterial subunit delta. J Struct Biol 207:199–208. https://doi.org/10.1016/j.jsb.2019.05.008.
11. Guo H, Courbon GM, Bueler SA, Mai J, Liu J, Rubinstein JL. 2021. Structure of mycobacterial ATP synthase bound to the tuberculosis drug bedaquiline. Nature 589:143–147. https://doi.org/10.1038/s41586-020-3004-3.
12. Harikishore A, Saw W-G, Ragunathan P, Litty D, Dick T, Müller V, Grüber G. 2022. Mutational analysis of mycobacterial F-ATP synthase subunit delta leads to a potent delta enzyme inhibitor. ACS Chem Biol 17:529–535. https://doi.org/10.1021/acschembio.1c00766.
13. Haagsma AC, Driessen NN, Hahn MM, Lill H, Bald D. 2010. ATP synthase in slow- and fast-growing mycobacteria is active in ATP synthesis and blocked in ATP hydrolysis direction. FEMS Microbiol Lett 313:68–74. https://doi.org/10.1111/j.1574-6968.2010.02123.x.
14. Hotra A, Suter M, Biuković G, Ragunathan P, Kundu S, Dick T, Grüber G. 2016. Deletion of a unique loop in the mycobacterial F-ATP synthase γ subunit sheds light on its inhibitory role in ATP hydrolysis-driven H+ pumping. FEBS J 283:1947–1961. https://doi.org/10.1111/febs.13715.
15. Ragunathan P, Sielaff H, Sundararaman L, Biuković G, Subramanian Manimekalai MS, Singh D, Kundu S, Wohland T, Frasch W, Dick T, Grüber G. 2017. The uniqueness of subunit α of mycobacterial F-ATP synthases: an evolutionary variant for niche adaptation. J Biol Chem 292:11262–11279. https://doi.org/10.1074/jbc.M117.784959.
16. Wong C-F, Grüber G. 2020. The unique C-terminal extension of mycobacterial F-ATP synthase subunit α is the major contributor to its latent ATP hydrolysis activity. Antimicrob Agents Chemother 64:e01568-20. https://doi.org/10.1128/AAC.01568-20.
17. Joon S, Ragunathan P, Sundararaman L, Nartey W, Kundu S, Manimekalai MSS, Bogdanović N, Dick T, Grüber G. 2018. The NMR solution structure of *Mycobacterium tuberculosis* F-ATP synthase subunit epsilon provides new insight into energy coupling inside the rotary engine. FEBS J 285:1111–1128. https://doi.org/10.1111/febs.14392.
18. Wong C-F, Lau A-M, Harikishore A, Saw W-G, Shin J, Ragunathan P, Bhushan S, Ngan S-FC, Sze SK, Bates RW, Dick T, Grüber G. 2021. A systematic assessment of mycobacterial F_1-ATPase subunit ε's role in latent ATPase hydrolysis. FEBS J 288:818–836. https://doi.org/10.1111/febs.15440.
19. Miranda-CasoLuengo AA, Staunton PM, Dinan AM, Lohan AJ, Loftus BJ. 2016. Functional characterization of the *Mycobacterium abscessus* genome coupled with condition specific transcriptomics reveals conserved molecular strategies for host adaptation and persistence. BMC Genomics 17:553. https://doi.org/10.1186/s12864-016-2868-y.
20. Andries K, Verhasselt P, Guillemont J, Göhlmann HWH, Neefs J-M, Winkler H, Van Gestel J, Timmerman P, Zhu M, Lee E, Williams P, de Chaffoy D, Huitric E, Hoffner S, Cambau E, Truffot-Pernot C, Lounis N, Jarlier V. 2005. A diarylquinoline drug active on the ATP synthase of *Mycobacterium tuberculosis*. Science 307:223–227. https://doi.org/10.1126/science.1106753.
21. Dupont C, Viljoen A, Thomas S, Roquet-Banères F, Herrmann J-L, Pethe K, Kremer L. 2017. Bedaquiline inhibits the ATP synthase in *Mycobacterium abscessus* and is effective in infected zebrafish. Antimicrob Agents Chemother 61:e01225-17. https://doi.org/10.1128/AAC.01225-17.
22. Hotra A, Ragunathan P, Ng PS, Seankongsuk P, Harikishore A, Sarathy JP, Saw W-G, Lakshmanan U, Sae-Lao P, Kalia NP, Shin J, Kalyanasundaram R, Anbarasu S, Parthasarathy K, Pradeep CN, Makhija H, Dröge P, Poulsen A, Tan JHL, Pethe K, Dick T, Bates RW, Grüber G. 2020. Discovery of a novel mycobacterial F-ATP synthase inhibitor and its potency in combination with diarylquinolines. Angew Chem Int Ed Engl 59:13295–13304. https://doi.org/10.1002/anie.202002546.
23. Ragunathan P, Dick T, Grüber G. 2022. Anti-*Mycobacterium abscessus* activity of tuberculosis F-ATP synthase inhibitor GaMF1. Antimicrob Agents Chemother 66:e00018-22. https://doi.org/10.1128/aac.00018-22.
24. Zhang AT, Montgomery MG, Leslie AGW, Cook GM, Walker JE. 2019. The structure of the catalytic domain of the ATP synthase from *Mycobacterium smegmatis* is a target for developing antitubercular drugs. Proc Natl Acad Sci U S A 116:4206–4211. https://doi.org/10.1073/pnas.1817615116.
25. Montgomery MG, Petri J, Spikes TE, Walker JE. 2021. Structure of the ATP synthase from *Mycobacterium smegmatis* provides targets for treating tuberculosis. Proc Natl Acad Sci U S A 118:e2111899118. https://doi.org/10.1073/pnas.2111899118.
26. Boyer PD. 1993. The binding change mechanism for ATP synthase—some probabilities and possibilities. Biochim Biophys Acta 1140:215–250. https://doi.org/10.1016/0005-2728(93)90063-L.
27. Noji H, Yasuda R, Yoshida M, Kinosita K, Jr. 1997. Direct observation of the rotation of F1-ATPase. Nature 386:299–302. https://doi.org/10.1038/386299a0.
28. Martin JL, Ishmukhametov R, Hornung T, Ahmad Z, Frasch WD. 2014. Anatomy of F_1-ATPase powered rotation. Proc Natl Acad Sci U S A 111:3715–3720. https://doi.org/10.1073/pnas.1317784111.
29. Gledhill JR, Montgomery MG, Leslie AGW, Walker JE. 2007. How the regulatory protein, IF_1, inhibits F_1-ATPase from bovine mitochondria. Proc Natl Acad Sci U S A 104:15671–15676. https://doi.org/10.1073/pnas.0707326104.
30. Morales-Ríos E, de la Rosa-Morales F, Mendoza-Hernández G, Rodríguez-Zavala JS, Celis H, Zarco-Zavala M, García-Trejo JJ. 2010. A novel 11-kDa inhibitory subunit in the F1FO ATP synthase of *Paracoccus denitrificans* and related α-proteobacteria. FASEB J 24:599–608. https://doi.org/10.1096/fj.09-137356.
31. Kobayashi R, Ueno H, Li C-B, Noji H. 2020. Rotary catalysis of bovine mitochondrial F_1-ATPase studied by single-molecule experiments. Proc Natl Acad Sci U S A 117:1447–1456. https://doi.org/10.1073/pnas.1909407117.
32. Hirono-Hara Y, Ishizuka K, Kinosita K, Yoshida M, Noji H. 2005. Activation of pausing F_1 motor by external force. Proc Natl Acad Sci U S A 102:4288–4293. https://doi.org/10.1073/pnas.0406486102.
33. Hirono-Hara Y, Noji H, Nishiura M, Muneyuki E, Hara KY, Yasuda R, Kinosita K, Yoshida M. 2001. Pause and rotation of F_1-ATPase during catalysis. Proc Natl Acad Sci U S A 98:13649–13654. https://doi.org/10.1073/pnas.241365698.
34. Harikishore A, Wong C-F, Ragunathan P, Litty D, Müller V, Grüber G. 2021. Targeting mycobacterial F-ATP synthase C-terminal α subunit interaction motif on rotary subunit γ. Antibiotics 10:1456. https://doi.org/10.3390/antibiotics10121456.
35. Gajadeera CS, Weber J. 2013. *Escherichia coli* F1Fo-ATP synthase with a b/δ fusion protein allows analysis of the function of the individual b subunits. J Biol Chem 288:26441–26447. https://doi.org/10.1074/jbc.M113.503722.
36. Saw W-G, Wong C-F, Dick T, Grüber G. 2020. Overexpression, purification, enzymatic and microscopic characterization of recombinant mycobacterial F-ATP synthase. Biochem Biophys Res Commun 522:374–380. https://doi.org/10.1016/j.bbrc.2019.11.098.
37. Wang F, Jain P, Gulten G, Liu Z, Feng Y, Ganesula K, Motiwala AS, Ioerger TR, Alland D, Vilchèze C, Jacobs WR, Sacchettini JC. 2010. *Mycobacterium tuberculosis* dihydrofolate reductase is not a target relevant to the antitubercular activity of isoniazid. Antimicrob Agents Chemother 54:3776–3782. https://doi.org/10.1128/AAC.00453-10.
38. Ho J, Sielaff H, Nadeem A, Svanborg C, Grüber G. 2015. The molecular motor F-ATP synthase is targeted by the tumoricidal protein HAMLET. J Mol Biol 427:1866–1874. https://doi.org/10.1016/j.jmb.2015.01.024.
39. Frishman D, Argos P. 1997. Seventy-five percent accuracy in protein secondary structure prediction. Proteins 27:329–335. https://doi.org/10.1002/(SICI)1097-0134(199703)27:3<329::AID-PROT1>3.0.CO;2-8.